PHYSICAL REVIEW FLUIDS **8**, 104604 (2023)

Wavelet-based modeling of subgrid scales in large-eddy simulation of particle-laden turbulent flows

M. Hausmann, F. Evrard,[*] and B. van Wachem[†]
Chair of Mechanical Process Engineering, Otto-von-Guericke-Universität Magdeburg,
Universitätsplatz 2, 39106 Magdeburg, Germany

(Received 17 May 2023; accepted 5 October 2023; published 24 October 2023)

We propose a model to obtain the subgrid-scale velocity in the context of large-eddy simulation (LES) of particle-laden turbulent flows, to recover accurate particle statistics. In our wavelet enrichment model, the subgrid-scale velocity is discretized with a divergence-free wavelet vector basis, and the coefficients of the expansion are obtained by minimizing the squared error of the linearized subfilter Navier-Stokes equations (SFNSE). The compact support of the wavelet basis is exploited to achieve continuously varying subgrid-scale velocity statistics across the domain. The performance of our wavelet enrichment model is evaluated in single-phase and particle-laden flow simulations, comparing the results with the results of direct numerical simulations (DNS). The simulations show that the model can generate inhomogeneous and anisotropic velocity statistics, accurate strain-rotation relations, and a good approximation of the kinetic energy spectrum of the corresponding DNS. Furthermore, the model significantly improves the prediction of the particle-pair dispersion, the clustering of the particles, and the turbulence modulation by particles in two-way coupled simulations. The proposed model recovers the most important interactions between fluid turbulence and the behavior of the particles, while maintaining the computational cost on the order of an LES.

DOI: 10.1103/PhysRevFluids.8.104604

I. INTRODUCTION

The understanding of the underlying physics of the interactions between turbulence and particles has attracted a lot of research interest for many decades, because of its ubiquity in natural and industrial processes. The only way to capture the most important complex phenomena of these multiphase flows numerically is to perform direct numerical simulation (DNS), which resolves the turbulent length- and timescales down to the Kolmogorov scales. In single-phase turbulence, extensive research and model development have enabled good predictions of turbulence statistics with computational costs significantly smaller than the costs of a DNS. One of the methods that achieves this is large-eddy simulation (LES), which resolves the large flow structures with the numerical grid while modeling the effect of the smaller, unresolved scales. The success of LES in single-phase turbulence does not apply to particle-laden flows, since various interactions between the phases are not captured by existing LES models.

The dispersion and preferential concentration of particles in the turbulent flow can be very different if they are transported with the filtered fluid velocity field instead of the fluid velocity

---

[*] Also at Sibley School of Mechanical and Aerospace Engineering, Cornell University, Ithaca, New York 14853, USA.

[†] berend.vanwachem@ovgu.de

field that contains the full turbulent spectrum [1–4]. A solution to this is to model the unresolved fluid velocity at each particle position.

The reconstruction of the subgrid-scale fluid velocity field, even in the absence of particles, has been a topic of interest for decades, which explains the large variety of existing models. The majority of these models, however, suffers from drawbacks that make them unsuitable for the application to particle-laden turbulent flows.

A well-known method to generate a fictitious subgrid-scale fluid velocity field is the kinematic simulation that approximates the fluid velocity field as a truncated Fourier series with coefficients that are chosen from a Gaussian distribution, such that a given kinetic energy spectrum is achieved, and the resulting velocity field is divergence-free [5–7]. Since real turbulence is typically not Gaussian and potentially statistically inhomogeneous and anisotropic, the kinematic simulation does not provide a realistic turbulent field. The subgrid-scale velocity field can also be reconstructed by fractal interpolation as proposed by Scotti and Meneveau [8]. Even though the model is computationally cheap, no physical knowledge of turbulence is incorporated. Domaradzki and Loh [9] proposed a velocity field extrapolation method for the velocity field on a refined grid using explicit filtering of the nonlinear advective term in the Navier-Stokes equations. Without further modification, however, the resulting velocity field is not divergence-free. Another family of models either solves the subfilter Navier-Stokes equations (SFNSE) with a simplifying numerical method such as, e.g., partially freezing the velocity field [10], or model the SFNSE itself [11–15]. Even though accurate predictions are reported, the models can be computationally expensive or may introduce assumptions that cannot be justified in some contexts [16].

Approaches that approximate turbulent velocity fields inspired the development of models for LES of particle-laden flows. A class of models emerged that solve a stochastic differential equation for every particle independently (see, e.g., Refs. [17–22]), which turns out to be versatile and computationally efficient. By construction, however, these models predict poor particle pair statistics, and their results strongly depend on the choice of model parameters [23]. Improved particle statistics are observed with models that apply a deconvolution operator on the LES velocity field [24–26], but these models merely modify the velocity field on the LES grid and do not augment the range of modeled scales. Bassenne *et al.* [27] combine the dynamical deconvolution of Park *et al.* [26] with the subgrid extrapolation of Domaradzki and Loh [9] and obtain realistic particle clustering with LES of homogeneous isotropic turbulence (HIT) and for a wide range of Stokes numbers. The high computational cost, originating from a divergence-free projection on a very fine grid, make this model unsuitable for LES. Recently, Hausmann *et al.* [28] proposed a model that solves the linearized SFNSE with Fourier basis functions in statistically homogeneous subdomains and apply it to particle-laden turbulent flows. In LES of HIT, the model mainly recovers particle pair dispersion and clustering of the corresponding DNS for particles of many Stokes numbers. Because of the statistically homogeneous subdomains, however, the subgrid-scale velocity field is partially discontinuous and requires interpolation.

In the present work, we derive a model for predicting the subgrid-scale fluid velocity field that recovers characteristic properties of turbulence, while maintaining computational costs that are acceptable in the scope of an LES. To obtain the right particle statistics and clustering, the modeled subgrid-scale velocity field is expected to have realistic spatial and temporal correlations, strain-rotation relations, and non-Gaussian distributions of, e.g., the fluid velocity gradients. A model for the subgrid-scale velocity must also be able to generate statistically inhomogeneous and anisotropic velocity fields.

In our model, the SFNSE are linearized by means of the rapid distortion theory and approximately solved by minimizing their squared error. The discrete solution spaces are spanned by divergence-free wavelet vector functions. The narrow support of the wavelet basis in physical and spectral space allows for spatially varying fluid velocity statistics and localization in spectral space, that is required to control the kinetic energy spectrum. Conceptually, the wavelet enrichment is superior to Fourier enrichment, which requires special treatment, such as statistically homogeneous subdomains, to generate an inhomogeneous subgrid-scale velocity field [15]. Divergence-free wavelet vector bases are also used by Letournel [29] to generate a turbulent velocity field by transporting the wavelet coefficients by a stochastic Langevin model. In the proposed model, however, a transport equation for the wavelet coefficients is derived that minimizes the error in the momentum balance. Other application of wavelets in reduced order turbulence modeling include the modeling of the subgrid-scale stress tensor in the scope of LES, by applying a wavelet transform to the resolved fluid velocity (see, e.g., Denev *et al.* [30]), which models the effect of the subgrid-scale velocity on the resolved scales but not the subgrid-scale velocity itself. A different approach involves performing LES with adaptive mesh refinement based on a wavelet decomposition of the resolved velocity. This approach employs thresholding to preserve only the most energetic scales, in contrast to the standard LES, which preserves only the largest scales (see, e.g., De Stefano and Vasilyev [31]). In contrast to the present work, however, the unresolved scales are not reconstructed. In a related study, Xiong *et al.* [32] study the particle statistics of particles transported with the fluid velocity field of an LES with wavelet-based adaptive mesh refinement (corresponding to the energetically optimal wavelet filtered DNS) and compare it to the statistics of particles transported with the fluid velocity field of a standard LES. It is concluded that the right particle statistics can be better recovered if the most energetic fluid velocity structures are used to transport the particles instead of the largest structures, which are resolved in a standard LES. In a subsequent study, they apply the dynamical deconvolution method of Park *et al.* [26] to the wavelet filtered DNS [33]. However, no model is proposed that can be applied to a standard LES to account for the unresolved fluid velocity field on the particle motion.

Even though the literature on LES of particle-turbulence interaction is dominated by studies and models for the subgrid-scale velocity at the particle positions, to enable one-way coupled simulations, more modeling is required in the case of two-way coupled simulations (i.e., where the turbulence modification by the particles is taken into account). Recently, Hausmann *et al.* [28] proposed a modeling framework that models the two-way coupling effects in an LES, caused by the unresolved fluid velocity field.

The paper is outlined as follows. The wavelet enrichment is derived in Sec. II, and the background of the governing equations and the wavelet basis is provided. In Sec. III, we introduce the simulation configuration that we use to evaluate the performance of the wavelet enrichment. The results and validation for single-phase and particle-laden flows are given in Sec. IV before the paper is concluded in Sec. V.

II. WAVELET MODEL FOR THE SUBGRID-SCALE VELOCITY

In this section, we describe the wavelet enrichment for the subgrid-scale velocity. The subgrid-scale fluid velocity field is projected onto a wavelet basis, and the coefficients of the expansion are determined by locally minimizing the mean-squared error of the linearized SFNSE.

A. Scale decomposition

LES is based on separating the flow into large-scale contributions and small-scale contributions. This is realized mathematically by filtering a quantity φ [34]:

$$\tilde{\varphi}(x) = \int_{-\infty}^{\infty} G(x-\xi)\varphi(\xi)d\xi, \tag{1}$$

where $\tilde{\cdot}$ indicates a filtered quantity and G is the filter kernel. Subfilter quantities are given by $\varphi' = \varphi - \tilde{\varphi}$, which we also refer to as subgrid-scale quantities in the scope of LES. Filtering the Navier-Stokes equations (NSE) of an incompressible fluid with constant density ρ_f and kinematic viscosity ν_f yields the filtered Navier-Stokes equations (FNSE):

$$\frac{\partial \tilde{u}_i}{\partial x_i} = 0, \tag{2}$$

$$\frac{\partial \tilde{u}_i}{\partial t} + \tilde{u}_j \frac{\partial \tilde{u}_i}{\partial x_j} = -\frac{1}{\rho_\mathrm{f}} \frac{\partial \tilde{p}}{\partial x_i} + \nu_\mathrm{f} \frac{\partial^2 \tilde{u}_i}{\partial x_j \partial x_j} - \frac{\partial \tau_{ij}}{\partial x_j} + \tilde{s}_i, \tag{3}$$

where u_i is the velocity and p is the pressure. The source term s_i represents, for instance, the momentum coupling of a second phase or a forcing to maintain statistically stationary turbulence. The subgrid-scale stress tensor accounts for the influence of the subgrid scales on the filtered scales and is given by

$$\tau_{ij} = \widetilde{u_i u_j} - \tilde{u}_i \tilde{u}_j. \tag{4}$$

By subtracting the FNSE from the NSE, the governing equations for the subgrid-scale fluid velocity are obtained. In models for the subgrid-scale velocity, the nonlinear term in the SFNSE is often omitted, or replaced by, a turbulent viscosity [11,12,14,15,35]. The resulting linearized SFNSE can be written as

$$\frac{\partial u_i'}{\partial x_i} = 0, \tag{5}$$

$$\frac{\partial u_i'}{\partial t} + \tilde{u}_j \frac{\partial u_i'}{\partial x_j} + u_j' \frac{\partial \tilde{u}_i}{\partial x_j} = -\frac{1}{\rho_\mathrm{f}} \frac{\partial p'}{\partial x_i} + (\nu_\mathrm{f} + \nu_\mathrm{t}') \frac{\partial^2 u_i'}{\partial x_j \partial x_j} + \frac{\partial \tau_{ij}}{\partial x_j} + s_i'. \tag{6}$$

The turbulent viscosity can be derived from renormalization groups [36]:

$$\nu_\mathrm{t}'(k) = \left(\nu_\mathrm{f}^2 + \frac{2}{5} \int_k^\infty q^{-2} E(q) dq \right)^{1/2} - \nu_\mathrm{f}, \tag{7}$$

where $E(k)$ is the kinetic energy spectrum of the wave number k. The replacement of the nonlinear term with a turbulent viscosity can be justified energetically and by means of their contribution to intermittency [35]. Similar to subgrid-scale models relying on the Boussinesq hypotheses, however, the linearization mistakenly assumes an alignment of the eigenvectors of the subgrid-scale stress tensor with those of the fluid velocity gradient tensor (see, e.g., Horiuti [37]). Therefore, the use of an eddy viscosity, may it be in the SFNSE or LES subgrid-scale models, are only justified energetically. Furthermore, the derivation of Eq. (7) relies on the assumption homogeneous isotropic turbulence [36]. We justify its use in inhomogeneous and anisotropic configurations by the fact that the small velocity scales, which are reconstructed in the proposed model, are typically much more homogeneous and isotropic than the large scales. This is a typical assumption for modeling the subgrid-scale stress tensor [16].

Similar to our recently proposed model, we aim to efficiently solve the linearized SFNSE to approximate the subgrid-scale fluid velocity field. Instead of expanding the subgrid-scale fluid velocity field in Fourier space [15], we approximate it as a finite series of wavelet basis functions. The rapidly decaying support of a wavelet basis in spectral and physical space enables a model that incorporates spectral space information and spatial inhomogeneities.

B. Multiresolution analysis

A Fourier series consists of basis functions (i.e., sines and cosines) that are perfectly localized in spectral space (they can be associated to exactly one wave number), but it has no localization in physical space (it is unknown where a frequency occurs). Convoluting the trigonometric basis functions of a Fourier series with a Gaussian window function enables localization of the spectral information in physical space. This is known as the discrete Gabor transform (see, e.g., Ref. [38]). Because of the constant window size, the low wave numbers tend to be spectrally underresolved and high wave numbers spatially underresolved. In fact, it is more appropriate to provide a wide physical support for small wave numbers and a narrow physical support for large wave numbers. A multiresolution analysis (MRA) applies this idea [38,39]. A MRA uses scaling functions ϕ and wavelets ψ as basis functions, that have compact support (or at least decay rapidly) in physical and spectral space. The scaling functions and the wavelets are elements of function spaces, which have specific properties. We consider subspaces of the Lebesgue space $(V_j)_{j\in\mathbb{Z}} \subset L^2(\mathbb{R})$, where the index j can be understood as an indicator of the range of wave numbers the functions possess that are deduced from the respective subspace. Functions that belong to subspaces of a large index j contain higher wave numbers than functions belonging to subspaces of a smaller index j. In the context of turbulence, that means that functions deduced from a subspace approximate eddies of a particular range of size, whereas a larger index corresponds to smaller eddies. The subspaces V_j have the following properties [39]:

(i) the subspaces are nested $V_j \subset V_{j+1}$,
(ii) their intersection is zero $\bigcap_{j\in\mathbb{Z}} V_j = \{0\}$,
(iii) $\bigcup_{j\in\mathbb{Z}} V_j$ is dense in $L^2(\mathbb{R})$,
(iv) they are invariant with respect to scaling $f \in V_j \iff f(2.) \in V_{j+1}$, and
(v) they are invariant with respect to translation $f \in V_j \Rightarrow f(. - k) \in V_j, \forall k \in \mathbb{Z}$.

One can imagine the functions of a subspace to represent a prototype eddy that is scaled in size, shifted in space, and superposed. Complementary spaces to V_j can be defined such that

$$V_{j+1} = V_j \oplus W_j. \tag{8}$$

Every function $f \in V_{j+1}$ is either $f \in V_j$ or $f \in W_j$, but not both. Consequently, we can decompose the $L^2(\mathbb{R})$ as

$$L^2(\mathbb{R}) = V_0 \bigoplus_{j=0}^{\infty} W_j. \tag{9}$$

From the so-called scaling function, or father wavelet, $\phi \in V_0$ and mother wavelet $\psi \in W_0$ functions are deduced such that V_j is spanned by $\{\phi_{jk}; j, k \in \mathbb{Z}\}$ and W_j is spanned by $\{\psi_{jk}; j, k \in \mathbb{Z}\}$:

$$\phi_{j,k}(\xi) = \phi(2^j\xi - k), \tag{10}$$

$$\psi_{j,k}(\xi) = \psi(2^j\xi - k). \tag{11}$$

Thus, a function $f \in L^2(\mathbb{R})$ may be expressed with a basis of scaling functions and wavelet functions

$$f(\xi) = \sum_{k\in\mathbb{Z}} c_{0,k}\phi_{0,k}(\xi) + \sum_{j\geqslant 0}\sum_{k\in\mathbb{Z}} d_{j,k}\psi_{j,k}(\xi). \tag{12}$$

Note that it is common to scale $\phi_{j,k}$ and $\psi_{j,k}$ with a factor of $2^{j/2}$. For simplicity, we absorb this factor in the coefficients $c_{0,k}$ and $d_{j,k}$.

The mother scaling function is defined by the low pass filter

$$\phi\left(\frac{\xi}{2}\right) = \sum_{k\in\mathbb{Z}} h_k\phi(\xi - k), \tag{13}$$

and the mother wavelet function is defined by the high pass filter

$$\psi\left(\frac{\xi}{2}\right) = \sum_{k\in\mathbb{Z}} g_k\phi(\xi - k). \tag{14}$$

The coefficients h_k, g_k characterize the different scaling functions and wavelets with different properties. We express the subgrid-scale velocity as a finite sum of divergence-free wavelet vector basis function as derived by Lemarié-Rieusset [40]

$$\boldsymbol{u}'(\boldsymbol{x}) = \sum_{j=j_{\min}}^{j_{\max}} \sum_{\boldsymbol{k}} \sum_{\epsilon} d^{\epsilon}_{\mathrm{div},j,\boldsymbol{k}} \boldsymbol{\Psi}^{\epsilon}_{\mathrm{div},j,\boldsymbol{k}}[\boldsymbol{\xi}(\boldsymbol{x})], \tag{15}$$

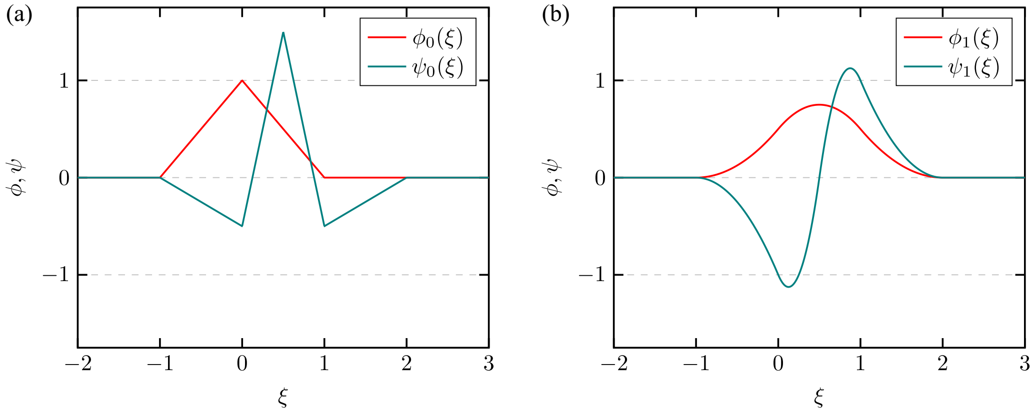

FIG. 1. Plot of the piecewise linear (a) and piecewise quadratic (b) spline scaling and wavelet functions.

where $d^{\epsilon}_{\text{div},j,\boldsymbol{k}}$ are the wavelet coefficients, $\boldsymbol{\Psi}^{\epsilon}_{\text{div},j,\boldsymbol{k}}$ are divergence-free wavelet vector basis functions, $j_{\min}$ and $j_{\max}$ the limits of the considered levels, and $\boldsymbol{\xi}(\boldsymbol{x})$ is a mapping from physical space coordinates $\boldsymbol{x}$ to the reference coordinates $\boldsymbol{\xi}$. The index ϵ specifies one of the 14 basis vector functions such that $\boldsymbol{\Psi}^{\epsilon}_{\text{div},j,\boldsymbol{k}}$ form a Riesz basis of the space of divergence-free vector functions in $\mathbb{R}^3$ [41]. Note that 21 basis vector functions are required to span the whole $\mathbb{R}^3$, and the projection onto the divergence free subspace reduces the number of basis vector functions to 14. The derivation of the basis functions and their exact expressions is relatively lengthy and can be found in Deriaz and Perrier [41]. Therefore, we do not repeat the derivation in the present work. The divergence-free vector functions are composed of four one-dimensional compactly supported spline functions that are depicted in Fig. 1 and defined by the coefficients h_k, g_k (in the proposed model similar to coefficients given by Deriaz and Perrier [41] but multiplied with a factor $\sqrt{2}$).

The mapping from physical coordinates to reference coordinates is given as

$$\xi_i(x_i) = (x_i - x_{i,\min})/(x_{i,\max} - x_{i,\min}), \tag{16}$$

where $x_{i,\min}$ and $x_{i,\max}$ are the limits of the cuboid domain. With the given mapping a periodic basis can be realized for $j \geqslant 3$, which is the first level with a support smaller than one.

C. Local least-squares approximation of the model equations

The subgrid-scale fluid velocity field lies within the space of divergence free vector functions in $\mathbb{R}^3$. Hence, it can be expressed as an infinite series of wavelet vector functions $\boldsymbol{\Psi}^{\epsilon}_{\text{div},j,\boldsymbol{k}}$ and coefficients $d^{\epsilon}_{\text{div},j,\boldsymbol{k}}$. We are searching coefficients of the finite series expansion Eq. (15), such that the subgrid-scale fluid velocity field is approximated well, which is divergence-free and conserves momentum at least by fulfilling the linearized momentum equation (6). With the expansion of the subgrid-scale velocity with the divergence-free vector functions, the former is satisfied immediately. The latter is achieved by a least-squares approximation, which is explained in the following.

The advective term in the linearized SFNSE can be Helmholtz decomposed in a divergence-free and a curl-free contribution. Since we seek a solution in the divergence-free wavelet vector space, the curl-free contribution can be dropped together with the pressure term, which gives

$$\frac{\partial u_i'}{\partial t} + \mathcal{A}_i^{\perp} = \mathcal{D}_i + \mathcal{F}_i^{\perp}, \tag{17}$$

where $\mathcal{A}_i^{\perp} = (\tilde{u}_j \frac{\partial u_i'}{\partial x_j} + u_j' \frac{\partial \tilde{u}_i}{\partial x_j})^{\perp}$ is an abbreviation for the projected advective term, $\mathcal{D}_i = (\nu_{\text{f}} + \nu_{\text{t}}') \frac{\partial^2 u_i'}{\partial x_j \partial x_j}$ for the diffusive term, and $\mathcal{F}_i^{\perp} = (\frac{\partial \tau_{ij}}{\partial x_j})^{\perp}$ for the projected forcing term, which originates from the subgrid-scale stress tensor and mainly supplies the subgrid-scale velocity field with kinetic energy (further details in Appendix B).

Minimizing the squared error of Eq. (17) over the whole domain results in the well known Galerkin method, which we refer to as globally optimal solution.

If the vector valued error of a differential equation at time t and point $\boldsymbol{x}$ is given as $\mathcal{E}_i(t,\boldsymbol{x})$, the optimal solution is achieved if

$$\int \mathcal{E}_i(t,\boldsymbol{x})\mathcal{E}_i(t,\boldsymbol{x})dV_x$$

is minimal. This can be achieved by adjusting the coefficients $d^{\epsilon}_{\mathrm{div},j,\boldsymbol{k}}$ of the discretized solution such that a stationary point is found, which corresponds to a minimum.

To make the solution for the coefficients affordable in the scope of an LES, we seek locally optimal solutions for every j and $\boldsymbol{k}$ independently:

$$\frac{\partial}{\partial d^{\zeta,n+1}_{\mathrm{div},j,\boldsymbol{k}}}\int\left[\frac{\boldsymbol{u}'^{,n+1}_{j,\boldsymbol{k}}-\boldsymbol{u}'^{,n}_{j,\boldsymbol{k}}}{\Delta t}+\boldsymbol{\mathcal{A}}^{\perp}_{j,\boldsymbol{k}}-\boldsymbol{\mathcal{D}}_{j,\boldsymbol{k}}-\boldsymbol{\mathcal{F}}^{\perp}_{j,\boldsymbol{k}}\right]^2 dV_x=0, \tag{18}$$

which yields the condition

$$\int\left[\frac{\boldsymbol{u}'^{,n+1}_{j,\boldsymbol{k}}-\boldsymbol{u}'^{,n}_{j,\boldsymbol{k}}}{\Delta t}+\boldsymbol{\mathcal{A}}^{\perp}_{j,\boldsymbol{k}}-\boldsymbol{\mathcal{D}}_{j,\boldsymbol{k}}-\boldsymbol{\mathcal{F}}^{\perp}_{j,\boldsymbol{k}}\right]\cdot\boldsymbol{\Psi}^{\zeta}_{\mathrm{div},j,\boldsymbol{k}}[\boldsymbol{\xi}(\boldsymbol{x})]dV_x=0. \tag{19}$$

The fluid velocity field local in j and $\boldsymbol{k}$, which we also refer to as local wave packets, is given as

$$\boldsymbol{u}'_{j,\boldsymbol{k}}(\boldsymbol{x})=\sum_{\epsilon} d^{\epsilon}_{\mathrm{div},j,\boldsymbol{k}}\boldsymbol{\Psi}^{\epsilon}_{\mathrm{div},j,\boldsymbol{k}}[\boldsymbol{\xi}(\boldsymbol{x})], \tag{20}$$

and $\boldsymbol{\mathcal{A}}^{\perp}_{j,\boldsymbol{k}}$, $\boldsymbol{\mathcal{D}}_{j,\boldsymbol{k}}$, and $\boldsymbol{\mathcal{F}}^{\perp}_{j,\boldsymbol{k}}$ are the projected advective, diffusive, and projected forcing term, as a function of the local velocity wave packets, respectively. The time derivative is discretized with an explicit Euler-scheme, where n indicates the time level.

Relaxing the global optimality condition to local $j,\boldsymbol{k}$ avoids the solution of a large equation system of size $14N_{\mathrm{k}}\times 14N_{\mathrm{k}}$. Instead, we invert N_{k} systems of size 14×14. Note that the matrix is always identical, and in practice only one inversion of the 14×14 matrix is required. The linear nature of the projected linearized SFNSE (17) allows for superposition of solutions, such as the approximated solutions for the local wave packets $\boldsymbol{u}'_{j,\boldsymbol{k}}(\boldsymbol{x})$. If the local wave packets would perfectly satisfy Eq. (17), then their superposition would also satisfy Eq. (17). Since $\boldsymbol{u}'_{j,\boldsymbol{k}}(\boldsymbol{x})$ is a numerical approximation, the discretization errors add up by superposing the solutions and, in total, lead to an error that is larger than the solutions of the global optimization using the Galerkin method. However, only with the localization of the optimization, and the associated increase of the numerical error compared to the Galerkin method, the solution for the subgrid-scale velocity field becomes computational feasible in the scope of LES. Together with the linearization of the SFNSE, the localization of the optimization constitutes the main assumption of our wavelet model.

Since the wavelet basis possesses no degrees of freedom in the space that is orthogonal to the divergence-free $[L^2(\mathbb{R}^3)]^3$, no explicit projection of the advective term is required to obtain a divergence-free subgrid-scale velocity. The projected advective term is obtained by expanding it in a series of wavelet basis functions (similar to the subgrid-scale velocity field) and solving the following problem:

$$\langle\boldsymbol{\mathcal{A}}^{\perp}_{j,\boldsymbol{k}}|\boldsymbol{\Psi}^{\epsilon}_{\mathrm{div},j,\boldsymbol{k}}\rangle=\langle\boldsymbol{\mathcal{A}}_{j,\boldsymbol{k}}|\boldsymbol{\Psi}^{\epsilon}_{\mathrm{div},j,\boldsymbol{k}}\rangle, \tag{21}$$

where $\langle .|.\rangle$ indicates the inner product. Equation (19) is solved with the resulting coefficients, which leads to the same discrete equations as using $\boldsymbol{\mathcal{A}}_{j,\boldsymbol{k}}$ without prior projection in Eq. (19).

Note the solution of Eq. (19) is guaranteed to produce the energetically optimal coefficients, because the Hessian

$$\mathcal{H}_{j,\boldsymbol{k}} = \mathcal{H}^{\epsilon,\zeta}_{j,\boldsymbol{k}} = \frac{\partial^2}{\partial d^{\epsilon,n+1}_{\mathrm{div},j,\boldsymbol{k}} \partial d^{\zeta,n+1}_{\mathrm{div},j,\boldsymbol{k}}} \int \left[\frac{\boldsymbol{u}'^{,n+1}_{j,\boldsymbol{k}} - \boldsymbol{u}'^{,n}_{j,\boldsymbol{k}}}{\Delta t} + \boldsymbol{\mathcal{A}}^{\perp}_{j,\boldsymbol{k}} - \boldsymbol{\mathcal{D}}_{j,\boldsymbol{k}} - \boldsymbol{\mathcal{F}}^{\perp}_{j,\boldsymbol{k}} \right]^2 dV_x$$
$$= \frac{2}{\Delta t^2} \int \boldsymbol{\Psi}^{\epsilon}_{\mathrm{div},j,\boldsymbol{k}}[\boldsymbol{\xi}(\boldsymbol{x})] \cdot \boldsymbol{\Psi}^{\zeta}_{\mathrm{div},j,\boldsymbol{k}}[\boldsymbol{\xi}(\boldsymbol{x})] dV_x, \tag{22}$$

is positive-definite, i.e., $\boldsymbol{v}^{\mathrm{T}} \mathcal{H}_{j,\boldsymbol{k}} \boldsymbol{v} > 0, \forall \boldsymbol{v} \in \mathbb{R}^{14} \setminus \{\boldsymbol{0}\}$. It follows that Eq. (18) constitutes a convex optimization problem and the solution has always a minimal error.

For a solution of Eq. (19) to exist, all terms of Eq. (19) must be integratable and finite, which means that the following expression have to be satisfied:

(i) $\int \boldsymbol{\Psi}^{\epsilon}_{\mathrm{div},j,\boldsymbol{k}}(\boldsymbol{x}) \cdot \boldsymbol{\Psi}^{\zeta}_{\mathrm{div},j,\boldsymbol{k}}(\boldsymbol{x}) dV_x < \infty$,

(ii) $\int \frac{\partial(\boldsymbol{\Psi}^{\epsilon}_{\mathrm{div},j,\boldsymbol{k}}(\boldsymbol{x}) \cdot \boldsymbol{\Psi}^{\zeta}_{\mathrm{div},j,\boldsymbol{k}}(\boldsymbol{x}))}{\partial x_j} dV_x < \infty$,

(iii) $\int \boldsymbol{\Psi}^{\epsilon}_{\mathrm{div},j,\boldsymbol{k}}(\boldsymbol{x}) \cdot \nabla^2 \boldsymbol{\Psi}^{\zeta}_{\mathrm{div},j,\boldsymbol{k}}(\boldsymbol{x}) dV_x < \infty$,

where $\boldsymbol{\Psi}^{\epsilon}_{\mathrm{div},j,\boldsymbol{k}}$ must possess second-order weak derivatives. The divergence-free basis introduced in Sec. II B satisfies these requirements.

D. Realization of the model in practice

The forcing term $\mathcal{F}_i$ represents the energy transfer from the resolved scales to the subgrid scales and is modeled in the proposed framework. A direct evaluation of $\mathcal{F}_i = \frac{\partial \tau_{ij}}{\partial x_j}$ requires explicit filtering with an a priori unknown filter. Kinetic energy can be added to the subgrid-scale velocity by the advective terms and the subgrid-scale stress tensor, that both underlie modeling assumptions (e.g., the linearization and the explicit filtering) and discretization errors. Consequently, undesired high or low kinetic energies can occur and even destabilize the numerical solution.

Since it is essential for the subgrid-scale velocity to have a realistic kinetic energy, we seek a model forcing term that can easily adjust the kinetic energy in both directions. The advective term $\mathcal{A}_i$ can add and remove kinetic energy across the scales. The diffusive term $\mathcal{D}_i$, however, always removes kinetic energy if the viscosity is positive. The advective term and the diffusive term are scaled to remove kinetic energy from or add kinetic energy to the subgrid-scale velocity field. The total viscosity is replaced by an effective viscosity:

$$\nu_{\mathrm{eff}}(k) = \sqrt{\frac{K_{j,\boldsymbol{k}}}{K_{j,\mathrm{desired}}}} [\nu_{\mathrm{f}} + \nu'_{\mathrm{t}}(k)]. \tag{23}$$

The kinetic energy of each wavelet is obtained with

$$K_{j,\boldsymbol{k}} = \frac{C_{d \to K}}{N_{\epsilon}} \sum_{\epsilon} \left(d^{\epsilon}_{\mathrm{div},j,\boldsymbol{k}}\right)^2, \tag{24}$$

where $C_{d \to K}$ is a constant that depends on the distribution of $d^{\epsilon}_{\mathrm{div},j,\boldsymbol{k}}$ and is frequently adjusted by rearranging Eq. (24) and sampling $K_{j,\boldsymbol{k}} = (\boldsymbol{u}'_{j,\boldsymbol{k}} \cdot \boldsymbol{u}'_{j,\boldsymbol{k}})/2$ at random positions. The desired kinetic energy follows the scaling of the spectrum of the inertial range

$$K_{j,\mathrm{desired}} = \frac{K_{\mathrm{desired}}}{\mathcal{N}} k_j^{-5/3} \Delta k_j, \tag{25}$$

with the norm

$$\mathcal{N} = \sum_j k_j^{-5/3} \Delta k_j, \tag{26}$$

and the wave number $k_j = 2^j 2\pi/L$. The wave number step is given by

$$\Delta k_j = \frac{k_{j+1} - k_{j-1}}{2}, \tag{27}$$

and L indicates the size of the domain. Since the basis functions are associated with a range of wave numbers, k_j must be interpreted as a characteristic wave number of the respective level j.

The advective term is also scaled with a factor of $\sqrt{K_{j,\text{desired}}/K_{j,\boldsymbol{k}}}$, which accelerates the adaption to the desired kinetic energy. This procedure for maintaining the kinetic energy is stable and insensitive to external disturbances, such as momentum sources originating from two-way coupled particles. Note that no forcing is introduced that prescribes a specific (typically Gaussian) probability distribution function (PDF).

As described in Sec. II B, the wavelet basis functions are shifted by discrete integer values in space. This leads to points in space that coincide with peaks of the basis functions and, consequently, to statistically higher kinetic energy at these points. To avoid such a spatial bias, the basis functions are not fixed in space but move with a velocity much smaller than the eddy-turnover time of the respective level and within a small region near their original position. There are many ways of realizing a random movement of the wavelets. The method we applied is described in Appendix A. Note that the movement of the wavelets solely requires modification of the sampling of the subgrid-scale velocity because the coefficients $d^{\epsilon}_{\text{div},j,\boldsymbol{k}}$ are determined independently for every j and $\boldsymbol{k}$.

In practice, the solution for the wavelet coefficients requires the evaluation of integrals, such as

$$\int \boldsymbol{\Psi}^{\epsilon}_{\text{div},j,\boldsymbol{k}}[\boldsymbol{\xi}(\boldsymbol{x})] \cdot \boldsymbol{\Psi}^{\zeta}_{\text{div},j,\boldsymbol{k}}[\boldsymbol{\xi}(\boldsymbol{x})] dV_x.$$

Other integrals also contain spatial derivatives of the wavelet basis functions. Since the basis functions do not change, the integrals can be computed only once and can be reused. The advective term requires the filtered fluid velocity and the filtered fluid velocity gradient. The interpolation of the filtered quantities to the position of the respective wavelet is the only interaction of the wavelet enrichment with the LES flow solver. This simple interpolation step can be realized across different types of flow solvers. Solving for the wavelet coefficients results in the solution of the following linear equation system for every j and $\boldsymbol{k}$:

$$\sum_{\zeta} A^{\epsilon,\zeta}_{j,\boldsymbol{k}} d^{\zeta}_{\text{div},j,\boldsymbol{k}} = b^{\epsilon}_{j,\boldsymbol{k}}, \tag{28}$$

where the coefficient matrix $A^{\epsilon,\zeta}_{j,\boldsymbol{k}}$ is of size 14 × 14 and identical for all j and $\boldsymbol{k}$. The right-hand side vector $b^{\epsilon}_{j,\boldsymbol{k}}$ contains the wavelet coefficients of the previous time step and interpolated LES quantities. Therefore, its values change every time step.

III. SIMULATION SETUPS

The predictions of the proposed wavelet enrichment model are evaluated by means of different single-phase and particle-laden flow configurations. In this section the numerical solution of the flow and the particle transport is briefly introduced, and the parameters of the simulations are provided.

A. Numerical solution

The NSE and FNSE are solved numerically for different configurations in cubic domains of size L and periodic boundary conditions in every direction. The subgrid-scale stress tensor in the LES is modeled with the localized dynamic kinetic energy model (LDKM) as proposed by Menon and coworkers [42,43] and extended to two-way coupled particle-laden flows by Hausmann *et al.* [28] (referred to as mLDKM). Note that the mLDKM requires a model for the subgrid-scale velocity at the positions of the particles to be closed. Besides the subgrid-scale stress tensor, the mLDKM also provides an estimation of the subgrid-scale kinetic energy considering the turbulence modulation

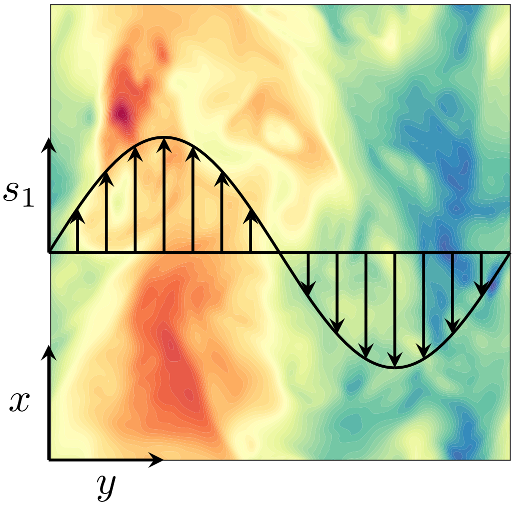

FIG. 2. Sketch of the turbulent shear flow configuration. A source term in x direction is added that varies with one period of a sin-profile across the y direction and drives a turbulent shear flow. The black arrows indicate the profile of the momentum source and the color represents a slice of the velocity in x direction.

by the particles. This subgrid-scale kinetic energy serves as K_{desired} for the wavelet enrichment in Eq. (25). Therefore, the generated subgrid-scale velocity considers, at least energetically, the turbulence modulation by the particles. Note that the effect of a changing slope of the kinetic energy spectrum is not accounted for. Altogether, the two-way coupling framework accounts for the influence of the subgrid-scale velocity on the particle transport, the influence of the particles on the resolved flow scales, and the effect of the particles on the subgrid scales. Details on how the two-way coupling interactions are modeled, can be found in Hausmann *et al.* [28]. A second-order finite volume solver is used to numerically solve the flow equations. More details on the flow solver may be found in Denner *et al.* [44] and Bartholomew *et al.* [45].

The investigated configurations differ in the source terms that appear in the momentum equations. We consider simulations of HIT, where a statistically steady state is obtained by continuously supplying kinetic energy through turbulence forcing. The forcing procedure is described in Mallouppas *et al.* [46].

A second type of flow investigated in this paper is a turbulent shear flow. This flow is simulated by a constant momentum source that varies as a sin-function across the domain:

$$\boldsymbol{s} = s_{\mathrm{max}} \sin(2\pi y/L)\boldsymbol{e}_1, \tag{29}$$

where s_{max} is the amplitude of the momentum source, and $\boldsymbol{e}_1$ is the basis vector in the x direction. For this turbulent shear flow configuration a shear Reynolds number is defined $\mathrm{Re}_{\mathrm{shear}} = L\sqrt{s_{\mathrm{max}}L}/\nu_{\mathrm{f}}$. A sketch of this configuration is provided in Fig. 2.

We also assess the wavelet enrichment model using a simulation configuration with two-way coupled point-particles, where the particle-induced momentum source is taken into account with the particle-source-in-cell (PSIC) method [47]

$$\boldsymbol{s} = -\frac{1}{\rho_{\mathrm{f}} V_{\mathrm{cell}}} \sum_{p \in \Omega_{\mathrm{cell}}} \boldsymbol{F}_p, \tag{30}$$

where Ω_{cell} represents a computational grid cell used in the finite volume solver that has a volume of V_{cell}. The particles are treated in a Lagrangian framework, and their motion is governed by the fluid-particle interface force, $\boldsymbol{F}_p$. We consider small, heavy, and spherical particles that we assumed to be only influenced by the drag force $\boldsymbol{F}_p = \boldsymbol{F}_{D,p}$, which we compute using Stokes' law augmented

TABLE I. Summary of the parameters that define the four simulations configurations.

Name	HIT-f-s	TS-s	HIT-f-1wc	HIT-d-2wc
Flow type	Forced HIT	turb. shear flow	Forced HIT	Decaying HIT
Energy supply	Turb. forcing	Sinusoidal force	Turb. forcing	–
Particles	–	–	One-way coupled	Two-way coupled
Taylor Reynolds number Re_λ	75	–	75	75
Turbulent Reynolds number Re_l	205	–	205	205
Shear Reynolds number $\mathrm{Re}_\mathrm{shear}$	–	3115	–	–
Reference time T_ref	$L/\sqrt{2/3\langle K\rangle}$	$\sqrt{L/s_\mathrm{max}}$	$L/\sqrt{2/3\langle K\rangle}$	$L/\sqrt{2/3\langle K\rangle}$
Kolmogorov length scale η/L	0.0017	0.0029	0.0017	0.0017
Kolmogorov timescale τ_η/T_ref	0.0075	0.026	0.0075	0.0075
Computational cells DNS N^3_DNS	256^3	128^3	256^3	256^3
Computational cells LES N^3_LES	32^3	16^3	32^3	32^3
Number of particles N_p	–	–	5 × 480 115	12 057 066
Stokes number St	–	–	0.5, 1, 2, 4, 8	8

with the Schiller-Naumann correlation [48]

$$\boldsymbol{F}_{\mathrm{D},p} = C_\mathrm{D}\frac{\rho_\mathrm{f}}{8}\pi d_p^2|\boldsymbol{u}_\mathrm{rel}|\boldsymbol{u}_\mathrm{rel}, \tag{31}$$

with the drag coefficient

$$C_\mathrm{D} = \frac{24}{\mathrm{Re}_p}\left(1+0.15\mathrm{Re}_p^{0.687}\right), \tag{32}$$

where d_p is the diameter of the particle with the index p and $\mathrm{Re}_p = \boldsymbol{u}_\mathrm{rel}d_p/\nu_\mathrm{f}$ is its Reynolds number. The relative velocity is the difference between the velocity of the particle $\boldsymbol{v}_p$ and the fluid velocity $\boldsymbol{u}(\boldsymbol{x}_p)$ at the position of the particle $\boldsymbol{x}_p$:

$$\boldsymbol{u}_\mathrm{rel} = \boldsymbol{u}(\boldsymbol{x}_p) - \boldsymbol{v}_p. \tag{33}$$

The particle position changes according to

$$\frac{d\boldsymbol{x}_p}{dt} = \boldsymbol{v}_p, \tag{34}$$

and the particle velocity according to Newton's second law

$$\frac{d\boldsymbol{v}_p}{dt} = \frac{1}{\rho_p V_p}\boldsymbol{F}_p, \tag{35}$$

where ρ_p is the density of the particle. The motion of the particles is obtained using the Verlet-scheme [49]. The fluid velocity is interpolated to the particle position by divergence-free interpolation [50].

B. Parameters of the simulations

We consider four different simulation configurations to assess the predictions of the proposed model: forced HIT of a single-phase flow (HIT-f-s), a single-phase turbulent shear flow (TS-s), forced HIT with one-way coupled particles of five different Stokes numbers (HIT-f-1wc), and decaying HIT with two-way coupled particles of Stokes number St = 8 and a particle mass fraction of $\phi_\mathrm{m} = 1$ (HIT-d-2wc). In Table I, important parameters of the four simulations are summarized. The flow quantities of the simulation HIT-d-2wc are given for the corresponding single-phase flow and before the onset of the decay of the turbulence.

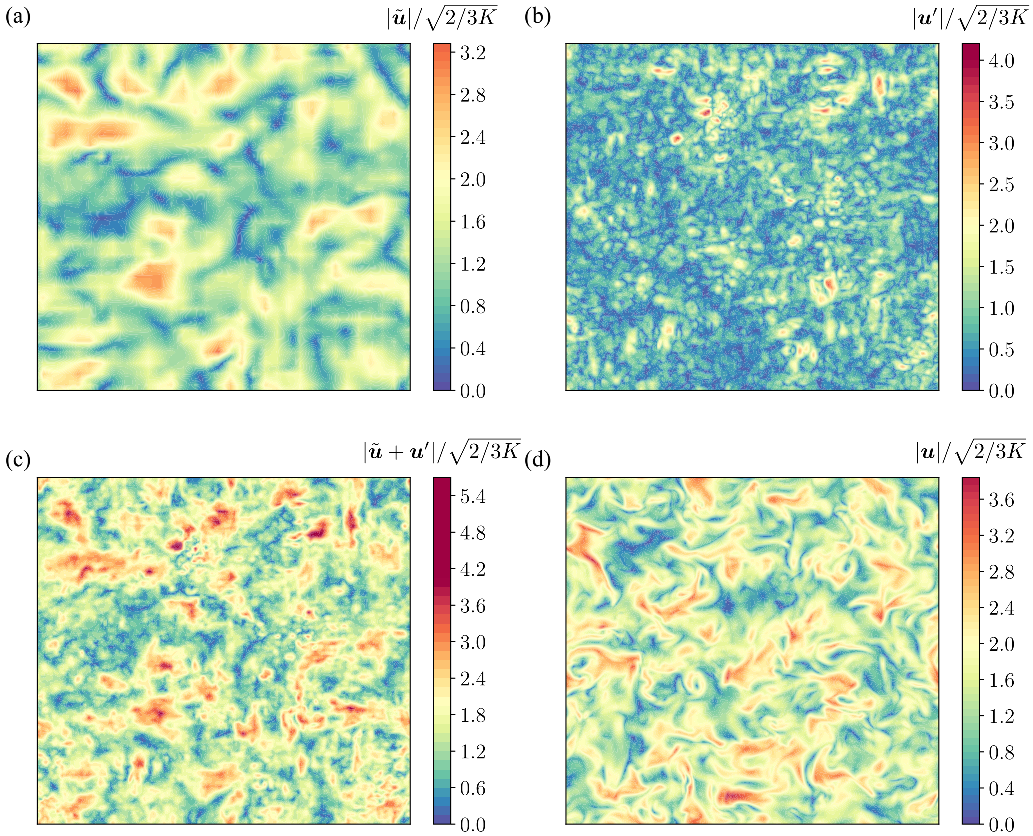

FIG. 3. Slice of the velocity magnitude for the simulation configuration HIT-f-s. The results are shown for the LES (a), the subgrid-scale velocity obtained from the wavelet enrichment (b), the superposition of the LES velocity and the the modeled subgrid-scale velocity (c), and the DNS (d). The color scaling of all subfigures is the same even though the maximum velocities are different.

The forcing is only applied in the wave number range $kL/2\pi \in [3, 6]$ for the forced HIT simulations. For the HIT simulations, the resolution is $k_{\max}\eta = 1.37$, and for the turbulent shear flow it is $k_{\max}\eta = 1.16$. The maximum resolved wave number is defined as $k_{\max} = \pi N_{\mathrm{DNS}}/L$.

In the LES of the HIT with the wavelet enrichment the range of considered levels is $j \in [4, 6]$ and in the LES of the turbulent shear flow $j \in [3, 5]$. The lowest levels are chosen such that their characteristic wave numbers correspond to the respective cutoff wave numbers of the LES. The upper level limits are chosen such that the significant amount of kinetic energy is captured with the modeled wave numbers.

IV. RESULTS AND DISCUSSIONS

In the present section we evaluate the predictions of the wavelet-enriched LES (LES-WL) and compare it to an LES without enrichment and the corresponding DNS. We separately discuss the single-phase flow statistics and the statistics of particle-laden flows.

A. Single-phase flow statistics

We first consider the flow statistics of the forced HIT configuration (HIT-f-s). Figure 3 compares the normalized fluid velocity magnitudes of the LES, the modeled subgrid-scale velocity obtained

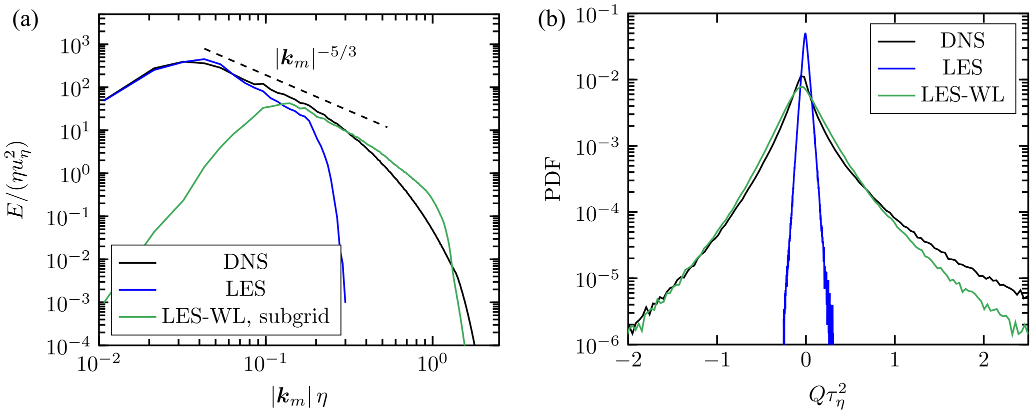

FIG. 4. Kinetic energy spectrum (a) and PDF of the second invariant of the velocity gradient tensor (b) for the simulation configuration HIT-f-s. The results are shown for the DNS, the LES, and the wavelet-enriched LES (LES-WL). The inertial range slope is plotted for comparison.

from the wavelet enrichment, and their sum with the DNS. The small flow structures, which are absent in the LES and provided by the wavelet enrichment, possess regions with different kinetic energies. This is possible because the compact support of the wavelet basis enables varying statistics across the domain. Some small regions with very high kinetic energy are observed. Such rare high intensity events are characteristic for turbulence and an indicator for intermittency. The superposition of the LES velocity and the modeled subgrid-scale velocity approximates the DNS velocity, which is widely similar in magnitude and range of length scales, but shows differences in the shape of the flow structures. The wavelet enrichment minimizes the local errors and, hence, prevents the systematical formation of flow structures with the neighbor wave packets.

The similarities of the velocity fields of the DNS and the wavelet-enriched LES can be quantified by comparing the kinetic energy spectra E normalized by the Kolmogorov length scale η and velocity u_η as shown in Fig. 4. The kinetic energy of the small wave numbers is recovered well by the LES. For the unresolved fluid velocity field the LES, the kinetic energy spectrum of the modeled subgrid-scale fluid velocity field approximates the kinetic energy spectrum of the DNS. Except for an overprediction of the spectrum of relatively small energy at high wave numbers, the general trend is captured. The observed deviation originates from the inertial range power law scaling prescribed by the forcing and may be improved if knowledge of the dissipation range is incorporated in the model.

As shown analytically by Maxey [51], the clustering of inertial particles of very small Stokes number is proportional to the second invariant of the fluid velocity gradient tensor

$$Q = \tfrac{1}{2}(\Omega_{ij}\Omega_{ij} - S_{ij}S_{ij}), \tag{36}$$

with the rotation-rate tensor Ω_{ij} and the strain-rate tensor S_{ij}. Therefore, to be able to correctly predict clustering, an accurate prediction of this tensor is crucial. Figure 4 shows the PDF of the second invariant of the velocity gradient tensor for the LES, the wavelet-enriched LES and the DNS. It can be observed that the LES by itself does not predict very high strain and low vorticity, or high vorticity and low strain events as is predicted by the DNS. With the wavelet-enriched LES, such events occur, even with a very similar probability as in the DNS; only the degree of asymmetry of the PDF (i.e., the higher probability of high rotation low strain events) is slightly underestimated as compared to the DNS. With the linearization of the SFNSE, the nonlinear term, as a contribution to the second invariant of the velocity gradient tensor, is modeled by a turbulent viscosity, that does not affect the second invariant of the velocity gradient tensor the same way as the nonlinear term.

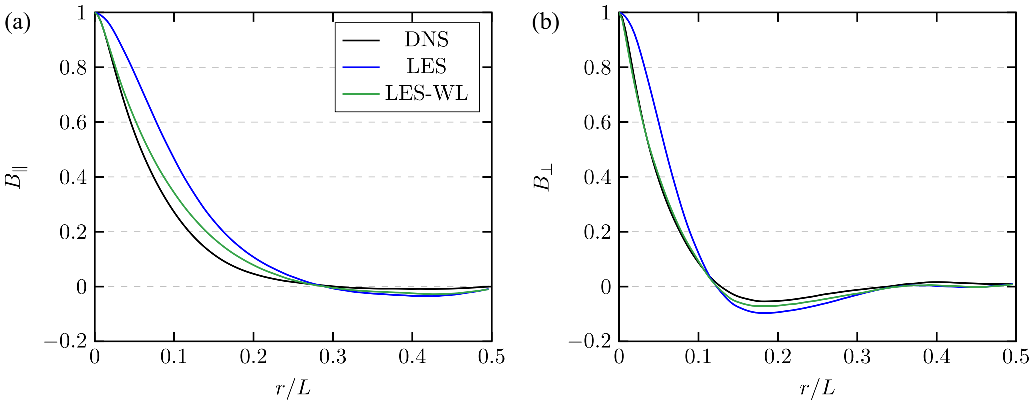

FIG. 5. Longitudinal (a) and transverse (b) fluid velocity autocorrelations over the distance r for the simulation configuration HIT-f-s. The results are shown for the DNS, the LES, and the wavelet-enriched LES (LES-WL).

This linearization can be an explanation for the observed deviation between the wavelet-enriched LES and the DNS.

Figure 5 shows the longitudinal and transverse fluid velocity autocorrelation functions, $B_\parallel$ and $B_\perp$, for the DNS, the LES without wavelet enrichment and the wavelet-enriched LES. For homogeneous isotropic flows, they are defined as [52]

$$B_\parallel(r) = \frac{\langle u_\alpha(\boldsymbol{x},t)u_\alpha(\boldsymbol{x}+r\boldsymbol{e}_\parallel,t)\rangle}{\langle u_\alpha(\boldsymbol{x},t)u_\alpha(\boldsymbol{x},t)\rangle}, \tag{37}$$

$$B_\perp(r) = \frac{\langle u_\alpha(\boldsymbol{x},t)u_\alpha(\boldsymbol{x}+r\boldsymbol{e}_\perp,t)\rangle}{\langle u_\alpha(\boldsymbol{x},t)u_\alpha(\boldsymbol{x},t)\rangle}, \tag{38}$$

where r denotes the distance between the evaluated fluid velocities and $\boldsymbol{e}_\parallel$ and $\boldsymbol{e}_\perp$ the unit vector in the longitudinal and transverse direction, respectively. Note that no summation is carried out over the index α.

It can be seen in Fig. 5, that the fluid velocity decorrelates faster in the transverse direction than in the longitudinal direction, which is qualitatively also captured by the two LES. The LES without wavelet enrichment, however, predicts too slow decorrelation of the velocity in the longitudinal and transverse direction. The decorrelation can be accelerated by the wavelet-enriched LES, as it provides the unresolved subgrid-scale velocity field. As a results, the autocorrelations of the wavelet-enriched LES are in very good agreement with the autocorrelations of the DNS for small distances r. As the distance increases, the energetic resolved eddies dominate the autocorrelation and the autocorrelations of the wavelet-enriched LES converge toward the autocorrelations of the LES without wavelet enrichment.

Figure 6 shows the PDF of the longitudinal and transverse velocity gradients, $A_{11} = \partial u_1/\partial x_1$ and $A_{12} = \partial u_1/\partial x_2$, normalized by their respective standard deviations, σ_{11} and σ_{12}. Similar to the DNS, the wavelet-enriched LES increases the probability of events of high magnitude of the gradients compared to the LES. The tails of the PDFs of the wavelet-enriched LES are wider than in a Gaussian distribution, which is also observed in the DNS. In the PDF of the transverse velocity gradients, the wavelet-enriched LES shows a good agreement with the shape of the DNS. For the longitudinal gradients, the PDF of the wavelet-enriched LES lacks asymmetry, but the overall agreement with the PDF of the DNS is significantly improved compared to the LES without wavelet enrichment.

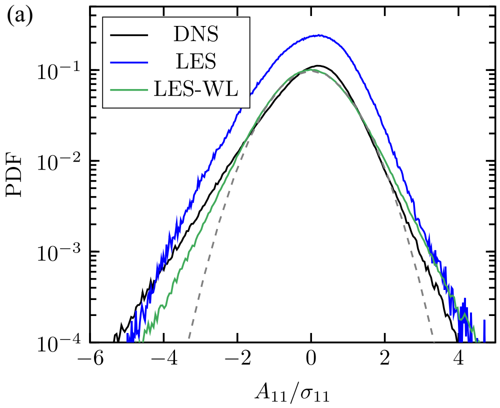

FIG. 6. PDF of longitudinal (a) and transverse (b) velocity gradients normalized by their standard deviations for the simulation configuration HIT-f-s. The results are shown for the DNS, the LES, and the wavelet-enriched LES (LES-WL). The dashed lines represent a Gaussian.

The analysis of the forced HIT proves that characteristic properties of turbulence can be reproduced by the wavelet enrichment, which cannot be achieved by, for instance, sampling random coefficient of Fourier-modes as done by a kinematic simulation (see, e.g., Zhou *et al.* [53]).

The computational cost of the wavelet-enriched LES for the simulation configuration HIT-f-s are approximately a factor 3–4 of the computational cost of the LES without enrichment. The computational cost of the corresponding DNS is four orders of magnitude higher.

Even though the wavelet enrichment proves to be capable of predicting realistic single-phase flow statistics in HIT, the vast majority of relevant flows in industry and nature is inhomogeneous and anisotropic. A simple inhomogeneous and anisotropic flow configuration is the turbulent shear flow (TS-s) introduced in Sec. III. In Fig. 7, we compare the spatial correlations of the subgrid-scale velocity, which are defined as

$$\mathcal{C}_{ij} = \langle (u_i' - \langle u_i' \rangle)(u_j' - \langle u_j' \rangle) \rangle, \tag{39}$$

where $\langle . \rangle$ indicates temporal averaging and averaging along the spatially homogeneous directions (i.e., x and z directions). The reference subgrid-scale fluid velocity field is obtained by subtracting

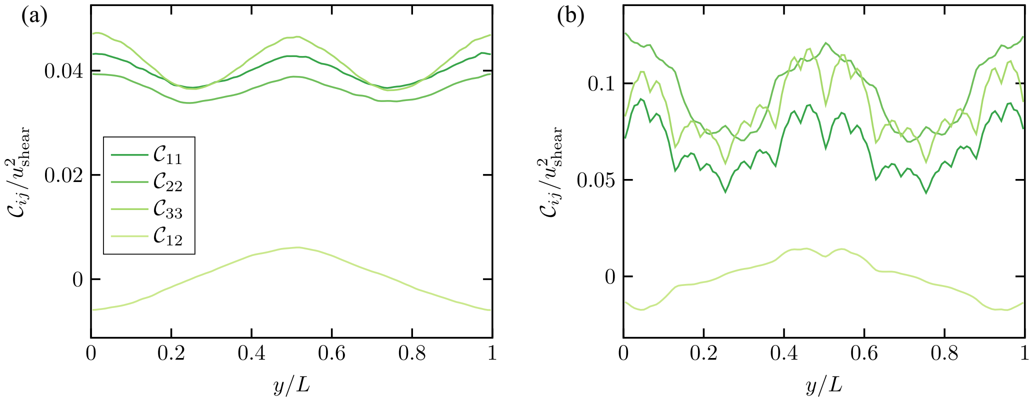

FIG. 7. Normalized spatial correlations in the y direction for the simulation configuration TS-s. (a) The correlations of the DNS explicitly filtered with a spectrally sharp filter and (b) the correlations of the subgrid-scale velocity that is modeled with the wavelet enrichment.

the explicitly filtered fluid velocity field of the DNS from the unfiltered fluid velocity field of the DNS, where a spectrally sharp filter is used. Because of the arbitrary choice of the filter, we compare the results only qualitatively.

It can be seen from Fig. 7 that the correlations of the wavelet enrichment are not as smooth as the correlations of the DNS. Because of the shape of the wavelet basis functions, regions occur that have statistically higher kinetic energy than other regions. Owing to the temporarily changing positions of the wavelet basis functions, which is explained in Sec. II D, the fluctuations are significantly reduced, but fluctuations remain in the ensemble averaged correlations that, however, are much smaller than the instantaneous velocity fluctuations.

The velocity correlations $\mathcal{C}_{11}$, $\mathcal{C}_{22}$, and $\mathcal{C}_{33}$ vary with two periods of a sine-shape across the y direction. With the wavelet enrichment this shape can be reproduced, albeit with different magnitudes, which can be traced back to the filter choice of the DNS and the estimation of the subgrid-scale kinetic energy. The cross-correlation $\mathcal{C}_{12}$ varies with one period of a sine-shape. At the domain center the velocities in the x and y directions are positively correlated and at the domain boundary negatively correlated. The wavelet enrichment reproduces this trend, which proves that the right anisotropic behavior can be generated from information that the wavelet enrichment receives from the LES.

B. Particle-laden flow statistics

We evaluate the particle statistics by comparing the results of forced HIT laden with one-way coupled particles (HIT-f-1wc). Figure 8 shows the particle pair dispersion, which is defined as the ensemble averaged temporal evolution of the distance between particle pairs with the position $\boldsymbol{x}_{p0}(t)$ and $\boldsymbol{x}_{p1}(t)$:

$$\langle\delta\rangle(t) = \langle|\boldsymbol{x}_{p0}(t) - \boldsymbol{x}_{p1}(t)|\rangle. \tag{40}$$

A particle pair is defined as two particles that have an initial separation of approximately the Kolmogorov length scale.

For all the considered Stokes numbers, three phases of the dispersion are observed in Fig. 8: (i) Particle pairs are located in the same eddy and stay close together, before (ii) they rapidly disperse by experiencing widely uncorrelated fluid velocities, and (iii) their maximum separation is reached, which is determined by the domain size. Since the LES only contains the largest eddies, that even the particles with the largest considered Stokes number can follow well, the dispersion is much slower than for the particles transported with the DNS velocity field. The wavelet-enriched LES leads to a particle pair dispersion that almost coincides with the DNS, for all considered Stokes numbers.

Most important for many applications is a correct prediction of particle clustering, i.e., that the particles preferentially concentrate in specific regions. A quantitative measure of particle clustering is provided by the radial distribution function, defined as

$$g(r) = \left\langle \frac{N_{\mathrm{p},i}(r)/\Delta V_i(r)}{N_{\mathrm{p}}/V} \right\rangle, \tag{41}$$

where $\Delta V_i(r)$ is the volume of spherical shells in a distance r, and $N_{\mathrm{p},i}(r)$ is the number of particle in the respective spherical shell. The radial distribution function is normalized with the total number of particles $N_{\mathrm{p},i}(r)$ and the total volume of the simulation domain V.

The radial distribution function in Fig. 9 predicted by the LES without wavelet enrichment significantly deviates from the radial distribution function predicted by the DNS, whereas the LES predicts too little clustering for $\mathrm{St} \in \{0.5, 1\}$ and too strong clustering for $\mathrm{St} \in \{2, 4, 8\}$. For the small Stokes numbers, the small eddies, that are absent in the LES without wavelet enrichment, move the particles toward regions of small vorticity and large strain. The particles with the larger Stokes numbers cannot follow the small eddies well. Consequently, the small fluid velocity structures increase the dispersion of the particles with large Stokes numbers. The correct prediction of clustering of the particles with small Stokes numbers is far more challenging, because

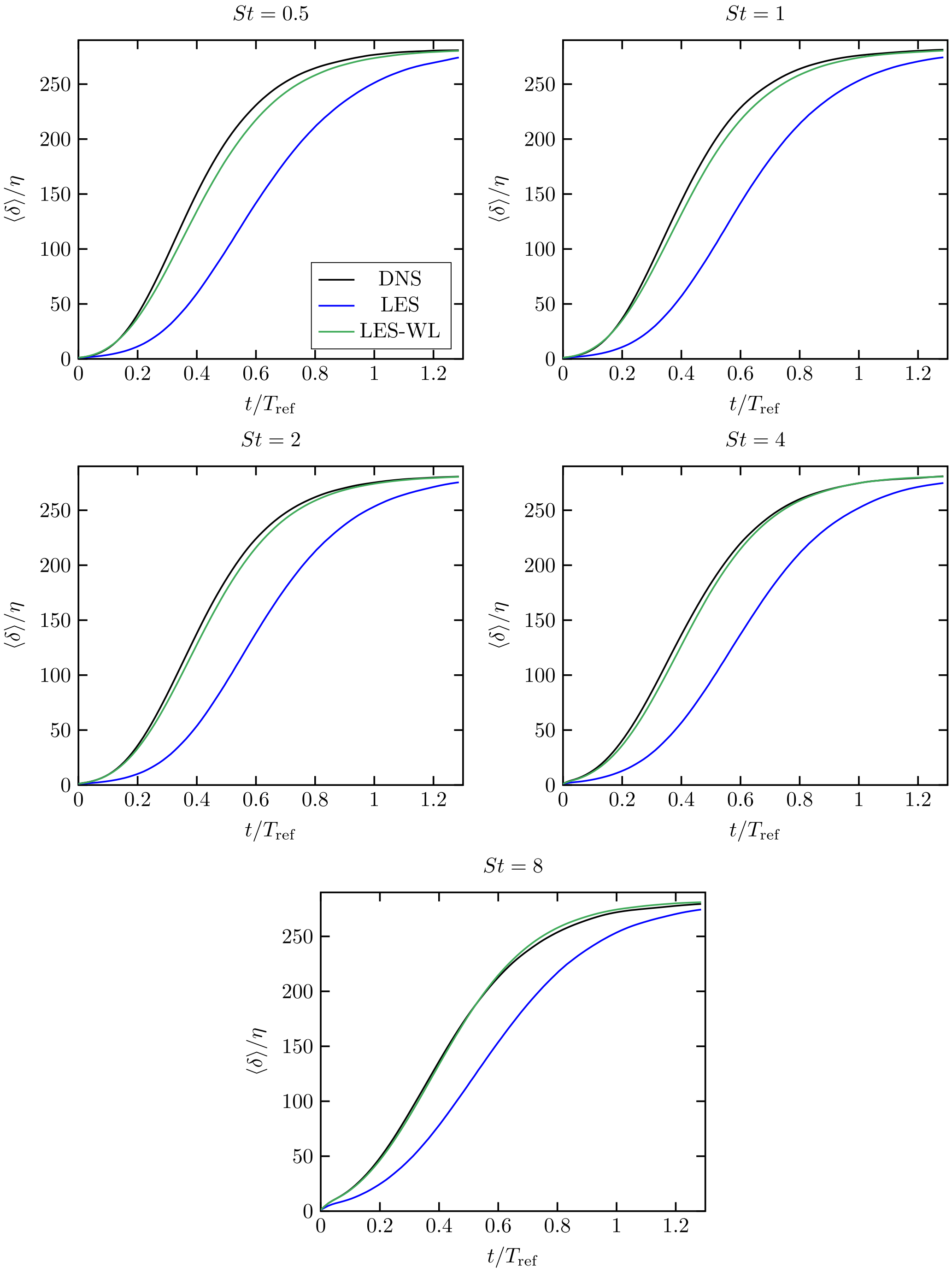

FIG. 8. Particle pair dispersion of particles with Stokes numbers in the range St ∈ {0.5, 1, 2, 4, 8} for the simulation configuration HIT-f-1wc. The considered particles pairs have an initial separation of the size of the Kolmogorov length scale η. The results are shown for the DNS, the LES, and the wavelet-enriched LES (LES-WL).

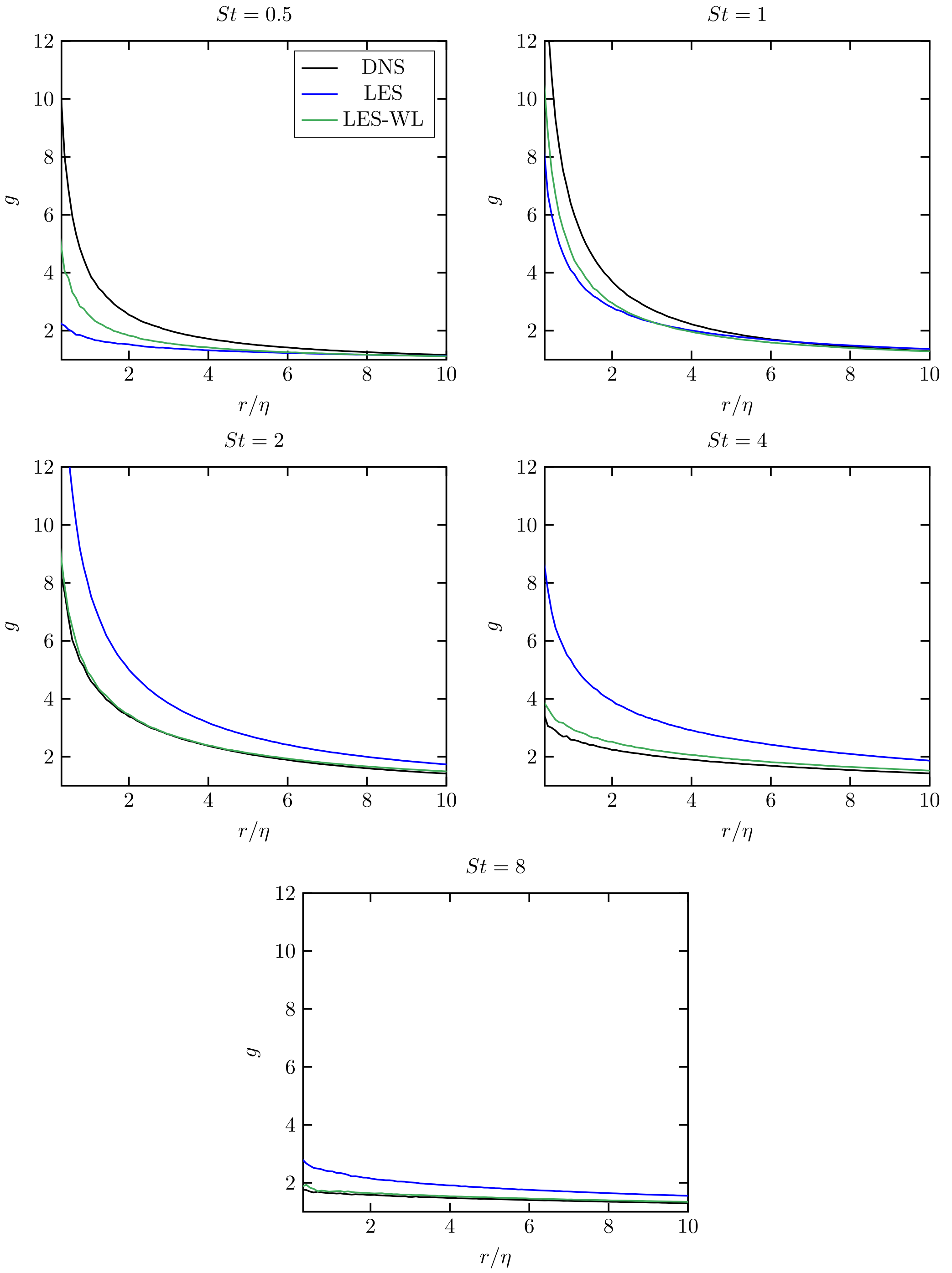

FIG. 9. Radial distribution function of particles with Stokes numbers in the range St ∈ {0.5, 1, 2, 4, 8} for the simulation configuration HIT-f-1wc. The results are shown for the DNS, the LES, and the wavelet-enriched LES (LES-WL).

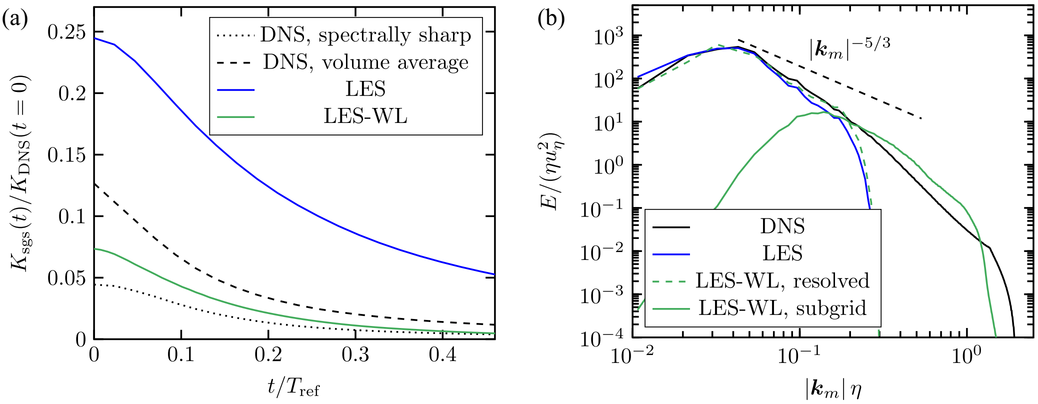

FIG. 10. Subgrid-scale kinetic energy over time (a) and kinetic energy spectrum before the onset of the decay (b) in decaying HIT laden with particles of Stokes number St = 8 for the simulation configuration HIT-d-2wc. The results are shown for the DNS, the LES, and the wavelet-enriched LES (LES-WL). The inertial range slope is plotted for comparison.

the strain-rotation relations of the small fluid velocity structures have a larger impact. It is observed in Fig. 9 that the wavelet-enriched LES significantly improves the radial distribution function for the Stokes numbers St $\geqslant 2$. The increased dispersion by the modeled subgrid-scale fluid velocity field yields an excellent agreement of the radial distribution function of the wavelet-enriched LES with the radial distribution function of the DNS. For the intricate case of Stokes numbers St = 0.5 and St = 1, only a relatively minor increase in particle clustering is observed.

The computational costs of the wavelet-enriched LES mainly depend on the levels, i.e., functions of the subspaces V_j that are considered and the number of particles that require sampling of the subgrid-scale velocity. The sampling of the subgrid-scale velocity at the positions of the particles is much more computationally expensive than computing the wavelet coefficients. The wavelet-enriched LES requires approximately twice the CPU-time for the HIT-f-1wc configuration than the Fourier enrichment [28]. This corresponds to approximately 10–15 times the CPU-time of the corresponding LES, which is significant, but still orders of magnitudes cheaper than a DNS.

The final test case considered in this paper considers two-way coupling. The abilities of the wavelet enrichment to predict the unresolved effects of two-way coupled particle-laden flows is assessed with the simulation configuration HIT-d-2wc, representing decaying HIT with two-way coupled particles with Stokes number St = 8. Figure 10(a) shows the temporal evolution of the subgrid-scale kinetic energy predicted by the LES without the wavelet enrichment and the LDKM, the wavelet-enriched LES with the mLDKM including the effect of the particles, and the DNS.

The reference subgrid-scale kinetic energy is obtained by explicit filtering the DNS. In an LES, the spatially varying turbulent viscosity imposes the filtering. This unknown filter leads to an uncertainty of the actual subgrid-scale kinetic energy. Therefore, the DNS is explicitly filtered with two different filters, a spectrally sharp filter and by volume averaging. During the whole decay the LES without wavelet enrichment and with the single-phase flow subgrid-scale model predicts a much too large subgrid-scale kinetic energy. The subgrid-scale model, i.e., the LDKM, assumes single-phase turbulence for the unresolved velocity scales, which contains more kinetic energy than the same flow laden with particles of Stokes number St = 8. Since the wavelet-enriched LES enables the use of the mLDKM that takes the turbulence modification by the particles into account, the predicted subgrid-scale kinetic energy is much smaller and lies between the subgrid-scale kinetic energy obtained from the DNS using the two different explicit filters. Note that the subgrid-scale kinetic energy obtained from the DNS is sensitive to the specific filter that is used.

The kinetic energy spectra before the onset of the decay are shown in Fig. 10(b). The turbulence modulation by the particles leads to a clear deviation of the DNS spectrum from the well known power-law of the inertial range that is observed in single-phase turbulence. Close to the cutoff wave number, the spectrum of the LES without wavelet enrichment using the LDKM deviates from the DNS spectrum because of the overestimated subgrid-scale kinetic energy and, thus, the too large turbulent viscosity. This is improved by the wavelet-enriched LES using the mLDKM that predicts a smaller turbulent viscosity and a better agreement with the kinetic energy spectrum of the DNS. The kinetic energy of the subgrid-scale velocity generated by the wavelet enrichment is slightly larger than the kinetic energy of the DNS. The shape of the kinetic energy spectrum, however, is very similar to the kinetic energy spectrum of the DNS.

V. CONCLUSIONS

We propose a model to predict the unresolved subgrid-scale fluid velocity field in the scope of an LES. In LES of particle-laden turbulent flows, the subgrid-scale velocity at the particle positions is required to predict correct particle behavior, such as their dispersion and clustering. Our wavelet enrichment model discretizes the subgrid-scale velocity by means of a divergence-free wavelet vector basis. The coefficients of this basis are obtained by minimizing the squared error of the linearized SFNSE. In contrast to structural models using a Fourier basis, the wavelet enrichment enables a continuous change of velocity statistics across the domain and, hence, the generation of an inhomogeneous subgrid-scale velocity field. Furthermore, the wavelet enrichment does not require to specify parameters that critically affect the results.

The model is validated with four distinct test cases that separately assesses the predictions of the wavelet enrichment in single-phase and particle-laden flows. Simulations of forced HIT show that the wavelet enrichment produces strain-rotation relations that are similar to the DNS. The PDFs of the longitudinal and transverse velocity gradients possess the expected non-Gaussian behavior. The wavelet enrichment is shown to be capable of predicting inhomogeneous and anisotropic velocity fields in a turbulent shear flow, where the spatial velocity correlations match those of DNS.

One-way coupled simulations of forced HIT of particles with different Stokes numbers revealed excellent agreement with the particle pair dispersion of the DNS. The predictions of particle clustering are improved, whereas the wavelet-enriched LES recovers the radial distribution function of the DNS very well for Stokes numbers $\mathrm{St} \geqslant 2$. By combining the wavelet enrichment with the recently proposed modification of the LDKM [28] to particle-laden flows, we report improved predictions of the subgrid-scale kinetic energy and the kinetic energy spectrum in two-way coupled decaying HIT.

The proposed wavelet enrichment is able to recover the most important interactions between turbulence and particles while maintaining computational costs of the order of the costs of an LES.

ACKNOWLEDGMENT

This research was funded by Deutsche Forschungsgemeinschaft (DFG, German Research Foundation) Project ID No. 457509672.

APPENDIX A: MOVEMENT OF THE WAVELETS

Let $\boldsymbol{x}_{j,\boldsymbol{k},\mathrm{c}}(t)$ be the coordinates of the center positions of the wavelets with the indices j and $\boldsymbol{k}$ that are initially given as

$$x_{i,j,\boldsymbol{k},\mathrm{c}}(t=0) = \frac{x_{i,\max} - x_{i,\min}}{2^j}(k_i + 1/2) + x_{i,\min}. \tag{A1}$$

A wavelet center is allowed to move within a region

$$\boldsymbol{x}_{j,\boldsymbol{k},\mathrm{c}}(t=0) - \boldsymbol{\delta}_j \leqslant \boldsymbol{x}_{j,\boldsymbol{k},\mathrm{c}}(t) \leqslant \boldsymbol{x}_{j,\boldsymbol{k},\mathrm{c}}(t=0) + \boldsymbol{\delta}_j, \tag{A2}$$

where

$$\delta_{i,j} = \frac{x_{i,\max} - x_{i,\min}}{2^{j+1}}. \tag{A3}$$

Within this region target coordinates $\boldsymbol{x}_{j,\boldsymbol{k},\mathrm{t}}$ are generated from a uniform distribution. The wavelet center moves toward the target coordinates with a constant velocity that is equal to 10% of the local eddy turnover time. As soon as the center coordinates are close to the target coordinates, new random target coordinates are generated

APPENDIX B: PROJECTION OF THE LINEARIZED SFNSE

This Appendix describes how the pressure term in the linearized SFNSE can be dropped if we solve it in the divergence-free subspace. We start from the linearized SFNSE

$$\frac{\partial u_i'}{\partial t} + \mathcal{A}_i = -\mathcal{P}_i + \mathcal{D}_i + \mathcal{F}_i, \tag{B1}$$

with the abbreviations

$$\mathcal{A}_i = \tilde{u}_j \frac{\partial u_i'}{\partial x_j} + u_j' \frac{\partial \tilde{u}_i}{\partial x_j},$$

$$\mathcal{P}_i = \frac{1}{\rho_\mathrm{f}} \frac{\partial p'}{\partial x_i},$$

$$\mathcal{D}_i = (\nu_\mathrm{f} + \nu_\mathrm{t}') \frac{\partial^2 u_i'}{\partial x_j \partial x_j}, \quad \text{and} \quad \mathcal{F}_i = \frac{\partial \tau_{ij}}{\partial x_j}.$$

Taking the divergence gives

$$\frac{\partial}{\partial x_i}\mathcal{P}_i = -\frac{\partial}{\partial x_i}\mathcal{A}_i + \frac{\partial}{\partial x_i}\mathcal{F}_i, \tag{B2}$$

because the divergence of the time derivative of the velocity and the diffusive term are zero, as it can be easily verified. Similarly, by taking the curl of Eq. (B1), we get

$$\mathrm{Curl}\left(\frac{\partial u_i'}{\partial t}\right) + \mathrm{Curl}(\mathcal{A}_i) = \mathrm{Curl}(\mathcal{D}_i) + \mathrm{Curl}(\mathcal{F}_i). \tag{B3}$$

Because the curl of a gradient is zero, the curl of the pressure term vanishes. According to the Helmholtz decomposition, the advective term and the forcing term can be decomposed into a divergence-free contribution, indicated with a $\perp$, and a curl-free contribution, indicated with the superscript curl, as follows:

$$\mathcal{A}_i = \mathcal{A}_i^{\perp} + \mathcal{A}_i^{\mathrm{curl}}, \tag{B4}$$

$$\mathcal{F}_i = \mathcal{F}_i^{\perp} + \mathcal{F}_i^{\mathrm{curl}}. \tag{B5}$$

Equation (B2) is satisfied if

$$\mathcal{P}_i = -\mathcal{A}_i^{\mathrm{curl}} + \mathcal{F}_i^{\mathrm{curl}}, \tag{B6}$$

and Eq. (B3) is satisfied if

$$\frac{\partial u_i'}{\partial t} + \mathcal{A}_i^{\perp} = \mathcal{D}_i + \mathcal{F}_i^{\perp}. \tag{B7}$$

Adding Eq. (B6) and Eq. (B7), gives the linearized SFNSE (B1). Equations (B6) and (B7) can be solved instead of solving the continuity equation together with Eq. (B1).

[1] V. Armenio, U. Piomelli, and V. Fiorotto, Effect of the subgrid scales on particle motion, Phys. Fluids **11**, 3030 (1999).

[2] B. Ray and L. R. Collins, Preferential concentration and relative velocity statistics of inertial particles in Navier–Stokes turbulence with and without filtering, J. Fluid Mech. **680**, 488 (2011).

[3] P. Fede and O. Simonin, Numerical study of the subgrid fluid turbulence effects on the statistics of heavy colliding particles, Phys. Fluids **18**, 045103 (2006).

[4] B. Rosa and J. Pozorski, Impact of subgrid fluid turbulence on inertial particles subject to gravity, J. Turbul. **18**, 634 (2017).

[5] R. H. Kraichnan, Diffusion by a random velocity field, Phys. Fluids **13**, 22 (1970).

[6] J. C. H. Fung, J. C. R. Hunt, N. A. Malik, and R. J. Perkins, Kinematic simulation of homogeneous turbulence by unsteady random Fourier modes, J. Fluid Mech. **236**, 281 (1992).

[7] N. A. Malik and J. C. Vassilicos, A Lagrangian model for turbulent dispersion with turbulent-like flow structure: Comparison with direct numerical simulation for two-particle statistics flow structure, Phys. Fluids **11**, 1572 (1999).

[8] A. Scotti and C. Meneveau, A fractal model for large-eddy simulation of turbulent flow, Physica D **127**, 198 (1999).

[9] J. A. Domaradzki and K.-C. Loh, The subgrid-scale estimation model in the physical space representation, Phys. Fluids **11**, 2330 (1999).

[10] M. Terracol, P. Sagaut, and C. Basdevant, A multilevel algorithm for large-eddy simulation of turbulent compressible flows, J. Comput. Phys. **167**, 439 (2001).

[11] B. Dubrulle, J. P. Laval, S. Nazarenko, and N. K.-R. Kevlahan, A dynamic subfilter-scale model for plane parallel flows, Phys. Fluids **13**, 2045 (2001).

[12] A. S. Ghate and S. K. Lele, Subfilter-scale enrichment of planetary boundary layer large-eddy simulation using discrete Fourier–Gabor modes, J. Fluid Mech. **819**, 494 (2017).

[13] T. J. Hughes, G. R. Feijóo, L. Mazzei, and J.-B. Quincy, The variational multiscale method—A paradigm for computational mechanics, Comput. Methods Appl. Mech. Eng. **166**, 3 (1998).

[14] T. J. Hughes, L. Mazzei, and K. E. Jansen, Large-eddy simulation and the variational multiscale method, Comput. Visual. Sci. **3**, 47 (2000).

[15] M. Hausmann, F. Evrard, and B. van Wachem, An efficient model for subgrid-scale velocity enrichment for large-eddy simulations of turbulent flows, Phys. Fluids **34**, 115135 (2022).

[16] P. Sagaut, *Large Eddy Simulation for Incompressible Flows*, 3rd ed. (Springer, Berlin, 2005).

[17] P. Fede, O. Simonin, P. Villedieu, and K. D. Squires, Stochastic modeling of the turbulent subgrid fluid velocity along inertial particle trajectories, in *Proceedings of the Summer Program* (2006), p. 247.

[18] M. Bini and W. P. Jones, Particle acceleration in turbulent flows: A class of nonlinear stochastic models for intermittency, Phys. Fluids **19**, 035104 (2007).

[19] A. S. Berrouk, D. Laurence, J. J. Riley, and D. E. Stock, Stochastic modelling of inertial particle dispersion by subgrid motion for LES of high Reynolds number pipe flow, J. Turbul. **8**, N50 (2007).

[20] B. Shotorban and F. Mashayek, A stochastic model for particle motion in large-eddy simulation, J. Turbul. **7**, N18 (2006).

[21] J. Pozorski and S. Apte, Filtered particle tracking in isotropic turbulence and stochastic modeling of subgrid-scale dispersion, Int. J. Multiphase Flow **35**, 118 (2009).

[22] M. Knorps and J. Pozorski, Stochastic modeling for subgrid-scale particle dispersion in large-eddy simulation of inhomogeneous turbulence, Phys. Fluids **33**, 043323 (2021).

[23] C. Marchioli, Large-eddy simulation of turbulent dispersed flows: A review of modelling approaches, Acta Mech. **228**, 741 (2017).

[24] J. G. M. Kuerten, Subgrid modeling in particle-laden channel flow, Phys. Fluids **18**, 025108 (2006).

[25] B. Shotorban and F. Mashayek, Modeling subgrid-scale effects on particles by approximate deconvolution, Phys. Fluids **17**, 081701 (2005).

[26] G. I. Park, M. Bassenne, J. Urzay, and P. Moin, A simple dynamic subgrid-scale model for LES of particle-laden turbulence, Phys. Rev. Fluids **2**, 044301 (2017).

[27] M. Bassenne, M. Esmaily, D. Livescu, P. Moin, and J. Urzay, A dynamic spectrally enriched subgrid-scale model for preferential concentration in particle-laden turbulence, Int. J. Multiphase Flow **116**, 270 (2019).

[28] M. Hausmann, F. Evrard, and B. van Wachem, Large-eddy simulation model for two-way coupled particle-laden turbulent flows, Phys. Rev. Fluids **8**, 084301 (2023).

[29] R. Letournel, Reduced-Order Modeling and Simulation of Turbulent Disperse Two-Phase Flows: New Theoretical and Modeling Approaches for Reproducing Intermittency, Segregation and Two-Way Coupling, Ph.D. thesis, Université Paris-Saclay, Paris, France, 2022.

[30] J. A. Denev, C. J. Falconi, J. Fröhlich, and H. Bockhorn, Wavelet-adapted subgrid-scale models for LES, in *Turbulence and Interactions*, Vol. 110, edited by E. H. Hirschel, W. Schröder, K. Fujii, W. Haase, B. Leer, M. A. Leschziner, M. Pandolfi, J. Periaux, A. Rizzi, B. Roux, Y. I. Shokin, M. Deville, T.-H. Lê, and P. Sagaut (Springer, Berlin, 2010), pp. 111–117.

[31] G. De Stefano and O. V. Vasilyev, Wavelet-based adaptive large-eddy simulation with explicit filtering, J. Comput. Phys. **238**, 240 (2013).

[32] Y. Xiong, J. Li, F. Fei, Z. Liu, and W. Luo, Influence of coherent vortex structures in subgrid-scale motions on particle statistics in homogeneous isotropic turbulence, Int. J. Multiphase Flow **113**, 358 (2019).

[33] Y. Xiong, R. Cai, J. Li, F. Fei, Z. Liu, and W. Luo, Structural subgrid-scale model based on wavelet filter for large-eddy simulation of particle-laden turbulence, Int. J. Multiphase Flow **143**, 103730 (2021).

[34] A. Leonard, Energy Cascade in Large-eddy simulations of turbulent fluid flows, in *Advances in Geophysics*, Vol. 18 (Elsevier, Amsterdam, 1975), pp. 237–248.

[35] J.-P. Laval, B. Dubrulle, and S. Nazarenko, Nonlocality and intermittency in three-dimensional turbulence, Phys. Fluids **13**, 1995 (2001).

[36] V. M. Canuto and M. S. Dubovikov, A dynamical model for turbulence. I. General formalism, Phys. Fluids **8**, 571 (1996).

[37] K. Horiuti, Roles of non-aligned eigenvectors of strain-rate and subgrid-scale stress tensors in turbulence generation, J. Fluid Mech. **491**, 65 (2003).

[38] S. L. Brunton and J. N. Kutz, *Data-Driven Science and Engineering: Machine Learning, Dynamical Systems, and Control*, 1st ed. (Cambridge University Press, Cambridge, UK, 2019).

[39] I. Daubechies, *Ten Lectures on Wavelets*, CBMS-NSF Regional Conference Series in Applied Mathematics No. 61 (Society for Industrial and Applied Mathematics, Philadelphia, PA, 1992).

[40] P. G. Lemarié-Rieusset, Analyses multi-résolutions non orthogonales, commutation entre projecteurs et derivation et ondelettes vecteurs à divergence nulIe, Rev. Mat. Iberoam. **8**, 221 (1992).

[41] E. Deriaz and V. Perrier, Divergence-free and curl-free wavelets in two dimensions and three dimensions: Application to turbulent flows, J. Turbul. **7**, N3 (2006).

[42] W.-W. Kim and S. Menon, An unsteady incompressible Navier-Stokes solver for large-eddy simulation of turbulent flows, Int. J. Numer. Methods Fluids **31**, 983 (1999).

[43] S. Menon, P.-K. Yeung, and W.-W. Kim, Effect of subgrid models on the computed interscale energy transfer in isotropic turbulence, Comput. Fluids **25**, 165 (1996).

[44] F. Denner, F. Evrard, and B. van Wachem, Conservative finite-volume framework and pressure-based algorithm for flows of incompressible, ideal-gas and real-gas fluids at all speeds, J. Comput. Phys. **409**, 109348 (2020).

[45] P. Bartholomew, F. Denner, M. Abdol-Azis, A. Marquis, and B. van Wachem, Unified formulation of the momentum-weighted interpolation for collocated variable arrangements, J. Comput. Phys. **375**, 177 (2018).

[46] G. Mallouppas, W. K. George, and B. van Wachem, New forcing scheme to sustain particle-laden homogeneous and isotropic turbulence, Phys. Fluids **25**, 083304 (2013).

[47] C. T. Crowe, M. P. Sharma, and D. E. Stock, The particle-pource-in cell (PSI-CELL) model for gas-droplet flows, J. Fluids Eng. **99**, 325 (1977).

[48] L. Schiller and A. Naumann, über die grundlegenden Berechnungen bei der Schwerkraftaufbereitung, Z. Ver. Dtsch. Ing. **77**, 318 (1933).

[49] L. Verlet, Computer "experiments" on classical fluids. I. Thermodynamical properties of Lennard-Jones molecules, Phys. Rev. **159**, 98 (1967).

[50] G. Tóth and P. Roe, Divergence- and curl-preserving prolongation and restriction formulas, J. Comput. Phys. **180**, 736 (2002).

[51] M. R. Maxey, The gravitational settling of aerosol particles in homogeneous turbulence and random flow fields, J. Fluid Mech. **174**, 441 (1987).

[52] W. K. George, Lectures in Turbulence for the 21st Century, Tech. Rep. (Department of Applied Mechanics, Chalmers University of Technology, Gothenburg, Sweden, 2010).

[53] Z. Zhou, S. Wang, X. Yang, and G. Jin, A structural subgrid-scale model for the collision-related statistics of inertial particles in large-eddy simulations of isotropic turbulent flows, Phys. Fluids **32**, 095103 (2020).